Joint Multifractal and Lacunarity Analysis of Image Profiles for Manufacturing Quality Control

Farhad Imani

Department of Industrial and Manufacturing Engineering, Pennsylvania State University,

State College, PA 16802 e-mail: fxi1@psu.edu

Bing Yao

Department of Industrial and Manufacturing Engineering, Pennsylvania State University, State College, PA 16802

e-mail: bzy111@psu.edu

Ruimin Chen

Department of Industrial and Manufacturing Engineering, Pennsylvania State University,

State College, PA 16802 e-mail: rxc91@psu.edu

Prahalad Rao

Department of Mechanical and Materials Engineering, University of Nebraska, Lincoln, NE 68588 e-mail: rao@unl.edu

Hui Yang¹

Department of Industrial and Manufacturing Engineering, Pennsylvania State University,

State College, PA 16802 e-mail: huy25@psu.edu

The modern manufacturing industry faces increasing demands to customize products according to personal needs, thereby leading to the proliferation of complex designs. To cope with design complexity, manufacturing systems are increasingly equipped with advanced sensing and imaging capabilities. However, traditional statistical process control methods are not concerned with the stream of in-process imaging data. Also, very little has been done to investigate nonlinearity, irregularity, and inhomogeneity in the image stream collected from manufacturing processes. This paper presents the joint multifractal and lacunarity analysis to characterize irregular and inhomogeneous patterns of image profiles, as well as detect the hidden dynamics in the manufacturing process. Experimental studies show that the proposed method not only effectively characterizes surface finishes for quality control of ultraprecision machining but also provides an effective model to link process parameters with fractal characteristics of in-process images acquired from additive manufacturing. This, in turn, will allow a swift response to processes changes and consequently reduce the number of defective products. The proposed multifractal method shows strong potentials to be applied for process monitoring and control in a variety of domains such as ultraprecision machining and additive manufacturing. [DOI: 10.1115/1.4042579]

Keywords: multifractal analysis, lacunarity, ultraprecision machining, additive manufacturing, process monitoring, image processing, quality control, surface finish

1 Introduction

Fierce competition in the global market pushes manufacturing companies to offer highly personalized products with complex designs to meet the customers' needs. This trend calls for the development of a next-generation manufacturing system that is highly flexible and adaptive to complex and customized designs. However, quality control of such complex products depends on advanced sensing, process monitoring, and control. For example, ultraprecision machining (UPM) is a commonly used manufacturing process to produce optical discs, photoreceptor components, and aircraft engines [1]. Such applications require mirror surface finishes with extremely high geometrical accuracies and smooth surfaces (i.e., surface roughness < 50 nm). Also, additive manufacturing (AM) provides a higher level of flexibility to print a 3D product with the complex geometry layer by layer. The laser powder bed fusion (LPBF)-AM process spreads the material powder over previous layers, and then uses a laser or electron beam energy source to melt the material powder to print a new layer of the product [2]. Qualifying complex builds is challenging. There is an urgent need to develop advanced quality control methods for monitoring layerwise finishes as we move into more complex and high-precision manufacturing [3].

Most of the complexity in the data arises from nonlinear and nonstationary dynamics of the manufacturing processes. Prior work showed the characterization of nonlinear dynamics in manufacturing systems and the resulted variations in products and systems performances [4]. Traditional statistical process control (SPC) methods mainly focus on key characteristics of the product and the conformance to specification, but are less concerned about highdimensional image data and nonlinear dynamics in manufacturing processes. Manufacturing system dynamics, confined by the evolution of states of the underlying process, exhibit aperiodic, strange, and irregular behaviors. Gültekin et al. [5] and Singer and Ben-Gal [6] showed that engineering control implementations often bring nonlinear dynamics of sensor observations in manufacturing processes.

There is a critical gap in the knowledge base that pertains to integrating nonlinear dynamics methods and tools with manufacturing quality control. Available nonlinear dynamics techniques are either not concerned with quality control objectives or fail to effectively analyze big data (e.g., high-dimension image data) to extract useful information for process control. There is an urgent need to harness and exploit nonlinear dynamics for creating new products (or services) with exceptional features such as adaptation, customization, responsiveness, and quality in unprecedented scales. The nonlinear dynamics theory focuses on the geometric properties of the state space of dynamical systems. For example, the fractal dimension is commonly used to describe the complex geometries of fractal objects (e.g., time series, 2D, or 3D images) that are self-similar and scale invariant. The fractal dimension can be a non-integer value that exceeds the topological dimension of the object.

However, a single fractal dimension focuses on the self-similarity (scale invariant) behavior of the fractal object and is limited in the ability to completely describe the multifractal patterns (i.e., non-linearity, irregularity, and inhomogeneity) in real-world objects. For example, image data from manufacturing processes often do not show perfect self-similarity but are formed by subsets with inhomogeneous scaling properties. The multifractal analysis is an effective tool to characterize inhomogeneous and nonlinear patterns of real-world images using an interwoven set of fractals with different dimensions. Furthermore, lacunarity complements multifractal analysis by characterizing the manner or distribution in which the fractal objects fill the space. Lacunarity and multifractal

¹Corresponding author.

Manuscript received March 20, 2018; final manuscript received January 2, 2019; published online February 27, 2019. Assoc. Editor: Dragan Djurdjanovic.

analysis jointly describe the irregularity and nonhomogeneity of fractal objects as well as how they fill the space that cannot be otherwise achieved by traditional fractal dimension or statistical features.

This paper presents the joint multifractal and lacunarity analysis of image profiles in UPM and AM processes for manufacturing quality control. The multifractal spectrum resolves local densities and captures nonhomogeneous variations of image profiles. Lacunarity complements multifractal analysis by characterizing the filling patterns in image profiles. Further, we derive the composite quality index by computing Hotelling T^2 statistics from multifractal and lacunarity features for defect detection and characterization in UPM and AM image profiles. Finally, we investigated the correlation between the Hotelling T^2 statistics and process parameters (i.e., hatch spacing, scan velocity, and laser power) in AM using regression analysis. Experimental results on real-world UPM and AM applications show that the proposed approach not only effectively detects and characterizes defects in image profiles but also provides an effective prediction model to link process parameters with image characteristics in AM processes.

2 Research Background

2.1 Manufacturing Processes and Advanced Imaging Technology. As shown in Fig. 1, UPM and AM processes are advanced manufacturing technologies that offer unique capabilities such as high precision and flexible customization that cannot be matched by traditional manufacturing techniques. UPM is equipped with air-bearing spindles and diamond tools to produce optical surface finishes (i.e., roughness \leq 50 nm). Also, the LPBF-AM process employs a laser power source for melting the material. The laser spot size is typically from 50 μ m to 100 μ m in diameter. The laser power is maintained in the range of 200–400 W, and the scan speed is varied in the range from 200 mm/s to 2000 mm/s [7].

Advanced sensing brings the increasing availability of high-dimensional images, which are critical to quality inspection and process improvement. For example, Fig. 1(a) shows the UPM surface extracted by high-resolution optical laser interference microscope (MicroXAM®). Figure 1(b) shows the industrial X-ray computed tomography (XCT) image for quality inspection of complex builds from LPBF-AM processes. Although UPM and AM offer exceptional capabilities, qualifying complex products are still

challenging. Very little has been done to study nonlinear and fractal patterns in real-world images and further exploit the useful information from high-resolution image data for the purpose of quality inspection.

2.2 Fractal Theory. In the natural world, there exist many irregular objects that show self-similarity to some degrees. For example, the human heart is formed of a fractal network of myocardium cells [8,9]. They are often referred to be the fractal geometry. The fractal theory has found many applications in many domains such as health informatics and manufacturing. Ruschin-Rimini et al. [10] developed a fractal-SPC method that uses the fractal dimension to measure the probability of the occurrence of correlated data sequences for process monitoring and change detection.

Further, manufactured surface finishes often exhibit fractal characteristics [11,12]. For example, UPM surface finishes seem to have smooth surfaces on visual inspection. However, fine-grained surface textures in the microscope demonstrate fractal behaviors over a range of scales. Fractal models provide insights into various functional and operational behaviors of manufacturing processes. In the literature, a single fractal dimension has been utilized to investigate the scale effect in surface metrology and consequently process monitoring [13,14]. Note that prior works showed that a single fractal dimension is limited in the ability to fully characterize heterogeneous and irregular patterns in the surface finishes from the manufacturing process. The surface finishes of manufactured parts often comprise of complex characteristics that are due to the existence of a spectrum of fractal dimensions that interact with each other to generate highly nonlinear behaviors. Very little has been done to integrate multifractal analysis with lacunarity patterns in image profiles for the purpose of quality monitoring and control of UPM and AM processes.

3 Research Methodology

3.1 Multifractal Analysis. Fractal objects are irregular and cannot be fully characterized by the topological dimensions. Therefore, the fractal dimension is introduced to describe scale-invariance properties of the fractal object by measuring the changes of covering relative to the scaling factor and characterizing the filling-space capacity. The box-counting method is widely utilized to estimate the fractal dimension of an irregular object. For example, if we

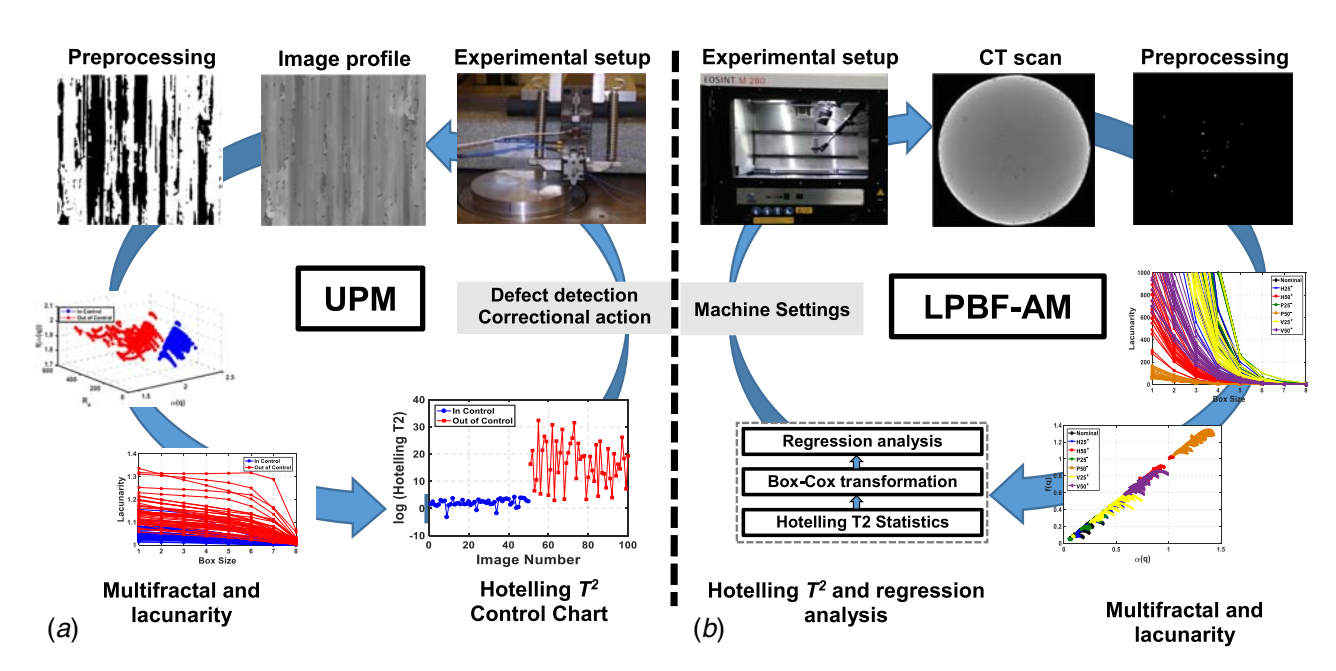


Fig. 1 Flow diagram of the research methodology: (a) UPM and (b) LPBF-AM processes

cover the fractal object by N measure elements (e.g., boxes) with size l as follows:

$$N(l) = l^{-D} \tag{1}$$

where D is the box-counting fractal dimension, then Eq. (1) provides the scaling law to demonstrate the distribution size of objects. This method covers a fractal set with measure elements (e.g., boxes) at different sizes and observes how the number of boxes varies with respect to the size [15]. This procedure is repeated using a different size of l. Once l becomes sufficiently small, the number of boxes N(l) is increased to cover a fractal object. Then the box-counting dimension D_0 becomes

$$D_0 = \lim_{l \to 0} \frac{\ln N(l)}{\ln(1/l)}$$
 (2)

To illustrate the self-similarity and irregularity in surface finishes, we used the Voronoi tessellation to iteratively divide a plane with points into convex polygons such that each polygon holds just one generating point and each point in a specified polygon is closer to its generating point than to any other (see Figs. 2(a)-2(c)). The dual of the Voronoi tessellation has been denoted as Delaunay triangulation (see Figs. 2(d)-2(f)).

As shown in Fig. 2, the images of Voronoi tessellation and Delaunay triangulation undergo significant changes when the number of cells is increased from 100 to 1000. The box-counting method computes the fractal dimension to be $D_0 = 2.089$ for both Voronoi and Delaunay images in Fig. 2. This indicates that a single fractal dimension is not sufficient enough to describe nonlinear and irregular behaviors. The box-counting method assumes that the number of boxes has a linear relationship with the box size when both are logarithmically transformed. To overcome this limitation, the multifractal analysis provides a more complete description of the irregular object with an interwoven set of fractal dimensions. The multifractal spectrum is computed as follows:

(a) Estimating the local density function

In practice, one way to quantify local densities is by estimating the mass probability in the *i*th box as follows:

$$P_i(l) = \frac{N_i(l)}{N_T} \tag{3}$$

(b) Calculating the singularity strength exponent

For the inhomogeneous set, we can define the singularity strength exponent α_i as follows:

$$P_i(l) \sim l^{\alpha_i} \tag{4}$$

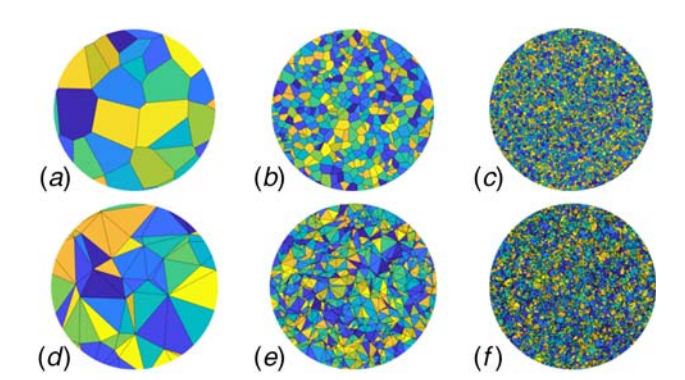


Fig. 2 Voronoi tessellation with different number of cells: (a) 100 cells, (b) 1000 cells, and (c) 10,000 cells; Delaunay triangulation with different number of cells: (d) 100 cells, (e) 1000 cells, and (f) 10,000 cells

size l and it can be estimated as follows: $\ln P_l(l)$

where α_i reflects the local behavior of $P_i(l)$ in the *i*th box with

$$\alpha_i = \lim_{l \to 0} \frac{\ln P_i(l)}{\ln l} \tag{5}$$

(c) Estimating the multifractal spectrum

The multifractal spectrum $f(\alpha)$ characterizes the variations and provides a statistical distribution of singularity exponents α_i . The number of boxes $N(\alpha)$ where the probability $P_i(l)$ has exponent values between α and $\alpha + d\alpha$ also follows the scaling law with the size l and multifractal spectrum $f(\alpha)$. It can be shown as follows:

$$N(\alpha) \sim l^{-f(\alpha)}$$
 (6)

The multifractal spectrum is a concave downward function due to two extreme properties of the measure (i.e., sparser or denser measure) and can be estimated from Eq. (6) as follows:

$$f(\alpha) = \lim_{L \to 0} \frac{\ln N(\alpha)}{\ln (1/l)} \tag{7}$$

The scaling of the qth moments of $P_i(l)$ distributions can be expressed as follows:

$$\sum_{i=1}^{N(l)} P_i^q(l) = l^{\tau(q)}$$
 (8)

where $\tau(q)$ is called the mass exponent of the qth order moment. Thus, the fractal dimensions D_q are written as follows:

$$D_q = \frac{\tau(q)}{q - 1} \tag{9}$$

When q = 0, Eq. (8) becomes $N(l) = l^{-D_0}$, which is similar to the box-counting dimension D_0 in Eq. (1). Further, the Legendre transformation is used to estimate the multifractal spectrum:

$$f(\alpha(q)) = q\alpha(q) - \tau(q) \tag{10}$$

$$\alpha(q) = \frac{d\tau(q)}{dq} \tag{11}$$

However, computing $f(\alpha(q))$ via Legendre transformation needs to smooth the D_q curve that causes errors to the estimated $f(\alpha)$. Equation (12) introduces a family of normalized measures $\mu_i(q, l)$ as qth moments of mass probability $P_i(l)$. A constant range of l is utilized to estimate multifractal properties over a small interval of scales.

$$\mu_i(q, l) = \frac{P_i^q(l)}{\sum_{i=1}^{N(l)} P_i^q(l)}$$
 (12)

As a result, the multifractal spectrum $f(\alpha(q))$ and average singularity strength exponent $\alpha(q)$ are obtained as follows:

$$f(\alpha(q)) = \lim_{l \to 0} \frac{\sum_{i=1}^{N(l)} \mu_i(q, l) \ln[\mu_i(q, l)]}{\ln l}$$
(13)

$$\alpha(q) = \lim_{l \to 0} \frac{\sum_{i=1}^{N(l)} \mu_i(q, l) \ln[P_i^q(l)]}{\ln l}$$
 (14)

where $f(\alpha(q))$ and $\alpha(q)$ are the function of the moments q. These two curves are tangent to each other at q=1. Figure 3 shows the multi-fractal spectrum and its major characteristics. The values in the right and left of D_0 represent negative and positive q values. Moments q>0 signify the contribution of boxes with higher-value

Journal of Manufacturing Science and Engineering

APRIL 2019, Vol. 141 / 044501-3

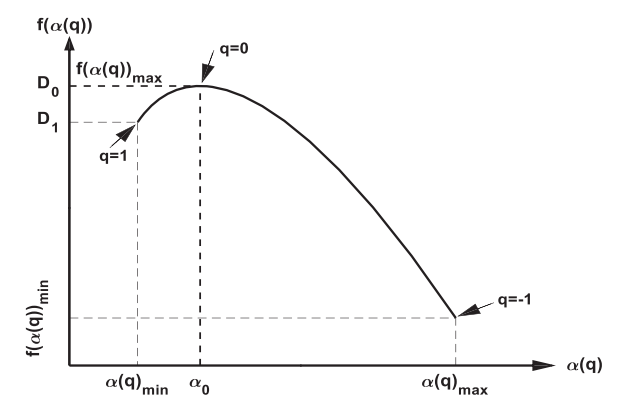


Fig. 3 Characteristic points in the multifractal spectrum

pixels in the estimates of $f(\alpha(q))$ and $\alpha(q)$. On the other hand, moments q < 0 signify the contribution of boxes with lower-value pixels in the estimation. Note that the right tail of $f(\alpha(q))$ is longer than the left side, which is mainly due to the fact that the variation of $f(\alpha(q))$ and $\alpha(q)$ with respect to q is more sensitive when q < 0.

3.2 Lacunarity. Further, lacunarity characterizes the filling-space capacity of fractals and textures that have the same fractal dimension and a very different visual appearance [16]. Lacunarity complements the multifractal analysis by determining how the fractal objects fill the space, thereby differentiating spatial patterns in different scales. We implement the computationally tractable "gliding box" method to compare the lacunarity [17]. A box of size l is placed in the image to count the number of set points s (black pixels). Then, this box is moved to another spot in the image, and the box mass is again counted. This process is repeated over the entire image, creating a frequency distribution of the box masses N(s, l). This distribution is converted into a probability distribution Q(s, l) by dividing by the total number of boxes N(l) of size l.

$$Q(s, l) = \frac{N(s, l)}{N(l)}$$

$$\tag{15}$$

The first and second moments of this distribution, as well as the lacunarity measure can be written respectively as follows:

$$Z^{(1)}(l) = \sum_{s} sQ(s, l)$$
 (16)

$$Z^{(2)}(l) = \sum_{s} s^{2} Q(s, l)$$
 (17)

$$\Lambda(l) = \frac{Z^{(2)}(l)}{(Z^{(1)}(l))^2}$$
 (18)

where $\Lambda(l)$ represents the lacunarity for the box size l. This procedure is repeated for different box sizes. If we have an image with G columns and G rows, the box size varies in the range of $2^1, \ldots, 2^b$ where $b < \log_2 G$. Then we obtain the log-scale plot of the lacunarity versus the box sizes.

Figure 4(a) shows the estimated multifractal spectra for Voronoi tessellation and Delaunay triangulation with 10,000 cells (see Fig. 2). Note that the single fractal dimension (i.e., the maximum values of $f(\alpha(q))$ is the same for both the images. However, their multifractal spectra are significantly different. The right tail of the Delaunay triangulation is longer than the dual Voronoi tessellation. This is due to the fact that the Delaunay triangulation has more pixels with lower values (intensity value toward 0 or black pixels) in comparison with the Voronoi tessellation. Figure 4(b) illustrates lacunarity spectra of the Voronoi tessellation with a different number of cells in Fig. 2. Note that the Voronoi tessellation with 100 cells has higher lacunarity values than the other two. This is mainly because lacunarity is related to the size distribution of the holes and deviation of an image from translational invariance. In other words, an object is very lacunar if its holes tend to be large and large gaps exist in an image. If there is a homogeneous image that has the same pixels per box, then the standard deviation, for a box count at the length scale l, will be close to the zero, and therefore lacunarity has a value close to zero.

3.3 Hotelling T^2 Control Chart of Multifractal and Lacunarity Features. The multifractal spectrum and lacunarity analysis provide a set of quality features relevant to the characteristics of surface finishes. For simultaneous monitoring of multidimensional features, hypothesis testing is used to determine whether there is a significant mean shift in the feature vector.

$$\mathbf{x}^{(i)} = \{ [\alpha(q_j), f(\alpha(q_j))]_{j=1...k}, \Lambda(l_w)_{w=1...b} \}^{(i)}, \quad i = 1, ..., m \quad (19)$$

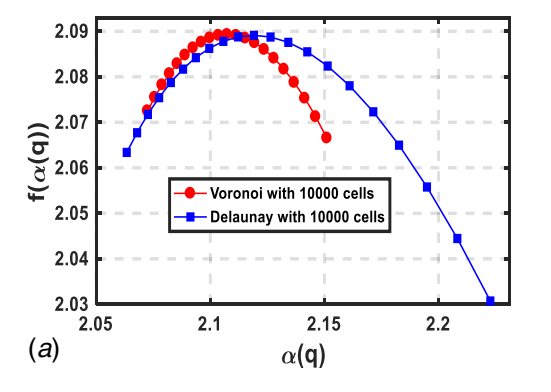
where $q_j \in [-1, 1]$, k is the size of the multifractal spectrum, b is the number of boxes in lacunarity, and m is the total number of images. The total number of features p is 2k + b, and the feature matrix is $X_{m \times p} = [x^{(1)}, x^{(2)}, \dots, x^{(m)}]^T$ with both multifractal and lacunarity quantifiers. To consider small changes in each direction of the multidimensional feature vector, we compute the Hotelling T^2 statistics for the ith image as follows:

$$T^{2}(i) = (x^{(i)} - \bar{x})S^{-1}(x^{(i)} - \bar{x})$$
(20)

where the sample mean vector \bar{x} and sample covariance matrix S are estimated from in-control or nominal data. The upper control limit of the Hoteling T^2 control chart is

$$UCL = \frac{p(m+1)(m-1)}{m(m-p)} F_{\alpha, p, m-p}$$
 (21)

where p is the dimensionality of $\mathbf{x}^{(i)}$, m is the number of images, $F_{\alpha,p,m-p}$ is the upper $100\alpha\%$ point of F distribution with p and



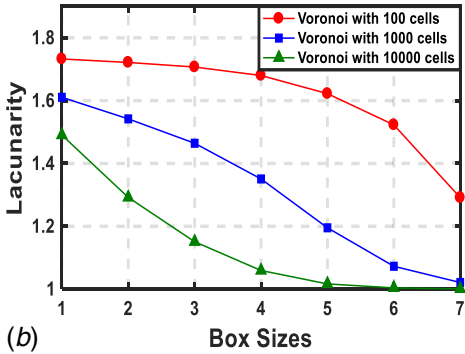


Fig. 4 (a) Multifractal spectra of the Voronoi tessellation and Delaunay triangulation in Fig. 2 and (b) lacunarity spectra of the Voronoi tessellation with different cells number in Fig. 2

m-p degrees of freedom. The Hotelling T^2 statistics is utilized to characterize the differences in surface finishes of UPM and LPBF-AM image profiles.

4 Experimental Design and Results

We evaluate and validate the proposed multifractal methodology in two real-world case studies for UPM and LPBF-AM image characterization and quality control. The first case study is aimed at evaluating the performance of multifractal and lacunarity for quality inspection of image profiles from the UPM process. In the second case study, we focus on modeling the relationship between process parameters with multifractal and lacunarity characteristics of XCT image profiles in the LPBF-AM process.

4.1 UPM Application. In the UPM process, R_a is the arithmetic average of the absolute intensity distance from each pixel to the mean [18]. As shown in Fig. 5, R_a provides the aggregated information and tends to be limited in the ability to fully characterize the surface. Figures 5(a) and 5(b) show two smooth surfaces with $R_a = 43.81$ nm and 43.83 nm, respectively. Also, Figs. 5(c) and 5(d) show two rough surfaces with $R_a = 297.58$ nm and 296.92 nm, respectively. Although R_a values are very close for two surfaces (either smooth or rough), their spatial patterns are different.

Figures 6 and 7 show the multifractal and lacunarity spectra for 4 UPM image profiles in Fig. 5, respectively. Note that multifractal

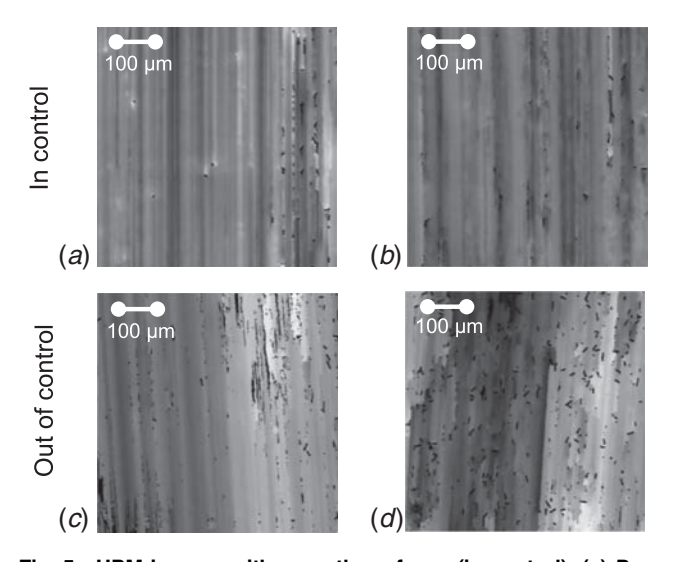


Fig. 5 UPM images with smooth surfaces (in-control): (a) R_a = 43.81 nm, (b) R_a = 43.83 nm and rough surfaces (out of control), (c) R_a = 297.58 nm, and (d) R_a = 296.92 nm

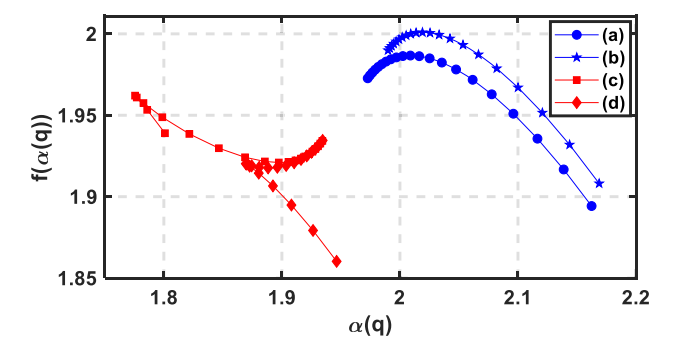


Fig. 6 Multifractal spectra of four UPM images: (a) R_a = 43.81 nm, (b) R_a = 43.83 nm, (c) R_a = 297.58 nm, and (d) R_a = 296.92 nm in Fig. 5

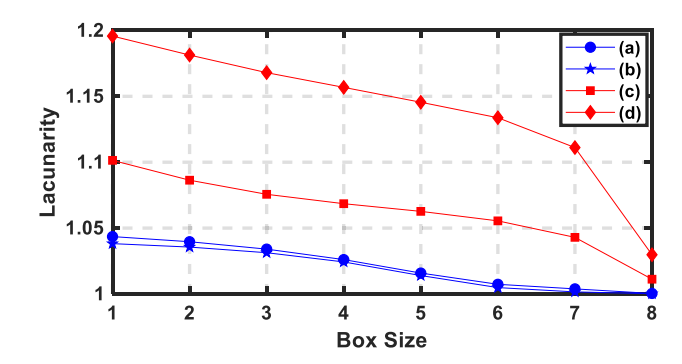


Fig. 7 Lacunarity spectra of 4 UPM images: (a) $R_a = 43.81$ nm, (b) $R_a = 43.83$ nm, (c) $R_a = 297.58$ nm, and (d) $R_a = 296.92$ nm in Fig. 5

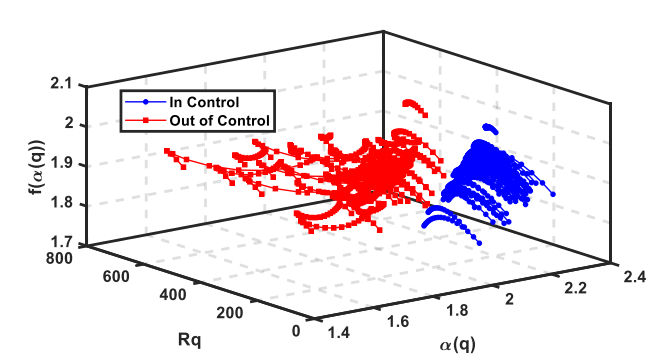


Fig. 8 Multifractal spectra of 100 UPM image profiles

and lacunarity spectra of smooth surfaces (i.e., $R_a \approx 43$ nm) are away from those of rough surfaces (i.e., $R_a \approx 297$ nm). For the surfaces with the same R_a values, multifractal and lacunarity spectra are close to each other but show differences because of the variations in spatial patterns.

Based on the threshold value of R_a = 100 nm, which is commonly considered for detecting the defects in the UPM process, 100 image profiles are split into the two groups of 50 in-control and 50 out-of-control. As shown in Fig. 8, image profiles from the in-control group show distinct multifractal spectra in comparison with those from the out-of-control group. Note that multifractal spectra of the in-control group are concave and they have higher values for $\alpha(q)$ in comparison with the out-of-control group. This is mainly due to the fact that there are more variation and heterogeneity in the inner layer of out-of-control images, which can be uniquely represented by the novel method of multifractal analysis.

Also, we extracted lacunarity measures to characterize the filling-space capacity of a multifractal object from the perspective of translational invariance. Figure 9 illustrates the lacunarity spectra of in-control and out-of-control UPM image profiles with respect to the number of boxes of different sizes. As shown in Fig. 9, the out-of-control images have higher lacunarity values for different box sizes in comparison with in-control image profiles. This shows that there are more gaps and heterogeneity in out-of-control image profiles.

Next, we characterize the differences in the multifractal spectrum $f(\alpha(q))$ and $\alpha(q)$ and lacunarity values of UPM image profiles by Hotelling T^2 statistics. Figure 10 demonstrates the logarithmic values of Hotelling T^2 for in-control and out-of-control image profiles. As shown in Fig. 10, Hotelling T^2 statistics of feature vectors show significant differences between in-control and out-of-control image profiles. Note that the negative values of log Hotelling T^2 statistics are related to Hotelling T^2 statistics that have values close to zero. The results show that multifractal and lacunarity analysis captures nonlinear variations inherent to an image profile by extracting

Journal of Manufacturing Science and Engineering

APRIL 2019, Vol. 141 / 044501-5

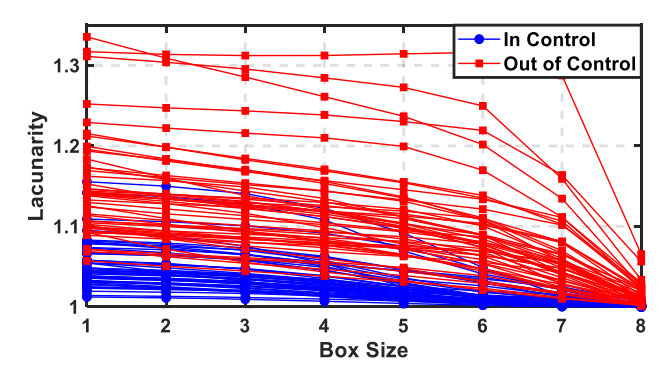


Fig. 9 Lacunarity spectra of UPM image profiles

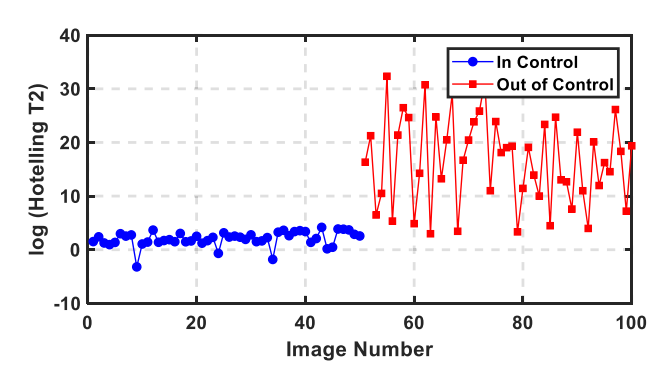


Fig. 10 The Hotelling T² chart of UPM image profiles

useful information from local densities and heterogeneous patterns in multiple scales.

4.2 LPBF-AM Application. This case study is to quantify the effects of process conditions on part porosity in laser LPBF-AM and then detect the onset of process conditions that lead to defects from in situ images. To this end, we developed a multivariate predictive model to investigate the effects of three LPBF-AM process parameters, namely, laser power (P), hatch spacing (H), and velocity (V) on the Hotelling T^2 values from image profiles. LPBF-AM experiments for this study were conducted using the EOS M280 machine along with spherical ASTM B348 Grade 23 Ti-6Al-4V powder whose particle size ranges from $14\mu m$ to $45 \mu m$.

The cylinder parts were printed with the design of experiments to vary the process parameters (see Fig. 11). Hatch spacing and laser scanning velocity are increased by 25% and 50% (i.e., 0.12 mm, 0.15 mm, and 0.18 mm for hatch spacing and 1250 mm/s, 1562.5 mm/s, and 1875 mm/s for scanning velocity). Laser power is decreased by 25% and 50% (i.e., 340 W, 250 W, and 170 W). We collected the 3D XCT scan data of cylinder parts built in the Applied Research Laboratory at The Pennsylvania State University. As the part is built layer by layer, we extract the 2D sliced images of each layer in the 3D printed cylinders. Our objective is to investigate how the change in process parameters impacts the porosity levels represented by Hotelling T^2 statistics for the layerwise image profile.

Figures 12(a) and 12(b) show the corresponding 3D XCT scan images and top view of the cylinder part which has a size of 25 mm in length and 10 mm in diameter. Figure 13 shows the multifractal spectra of 144 images under different printing conditions. The variations of process conditions lead to distinct multifractal spectra distributed in a wider range. Each set of process parameters leads to a group of multifractal spectra that are different from each other. The multifractal spectrum located the farthest from other groups in the top right corner of Fig. 13 is corresponding to the 50% decrease in power (i.e., P50-), which implies that higher

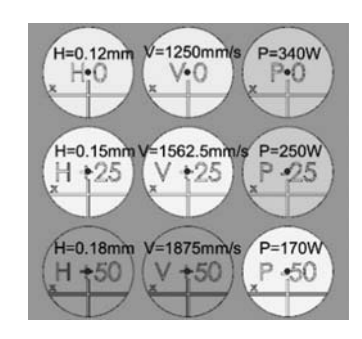


Fig. 11 Process parameter setting of the LPBF-AM cylinders

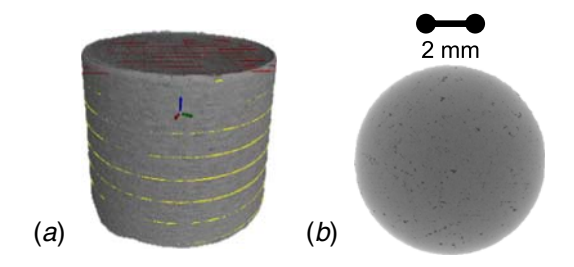


Fig. 12 $\,$ (a) 3D visualization of the XCT scan and (b) the top view of the XCT scan of a cylinder part

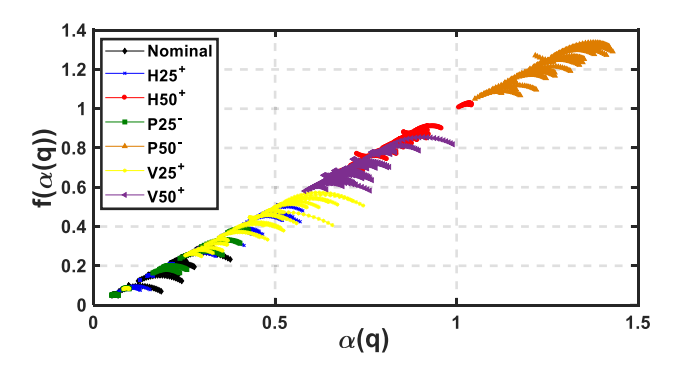


Fig. 13 Multifractal spectra of XCT scan images of the LPBF-AM process

heterogeneity exists in the layers of AM parts under this process setting. Also, the increase in hatch spacing and velocity leads to the multifractal spectra that are different from the nominal condition (i.e., (H0; V0; P0)). Such experimental results show that multifractal characteristics effectively reveal hidden features in LPBF-AM images that are strongly correlated with the variations of process parameters.

Figure 14 shows the lacunarity spectra of 144 XCT scan images of the LPBF-AM process. When the spectra of lacunarity values are small, the images show more heterogeneity. In other words, the increase in laser power has the most significant impact on causing more pores or defects on that layer. The second important factor pertinent to defects in the LPBF-AM process is the increase in hatch spacing. The joint lacunarity and multifractal results show that the proposed methodology is effective to identify the defects caused by variations in process parameters and has strong potentials to help control the system or take the correction action before the defects are extended to the next layers in the LPBF-AM process.

Further, we develop a regression model to investigate the relationship between process parameters with the Hotelling T^2 statistics, which is calculated based on the combined multifractal and lacunarity features of XCT image profiles. Here, the response variable y

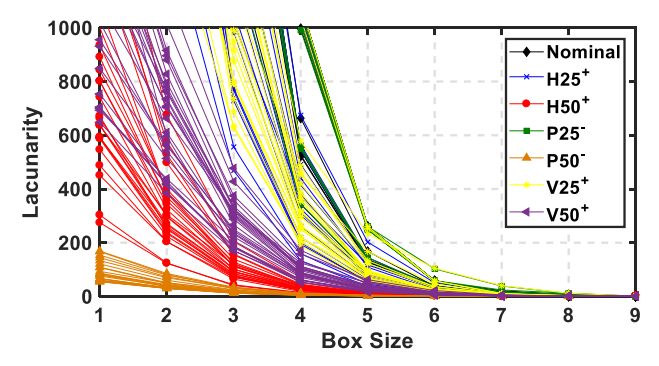


Fig. 14 Lacunarity spectra of XCT scan images of the LPBF-AM process

Table 1 R-squared values for the regression model

R-squared	R-squared (adjusted)	R-squared (predicted)
94.98%	94.76%	94.44%

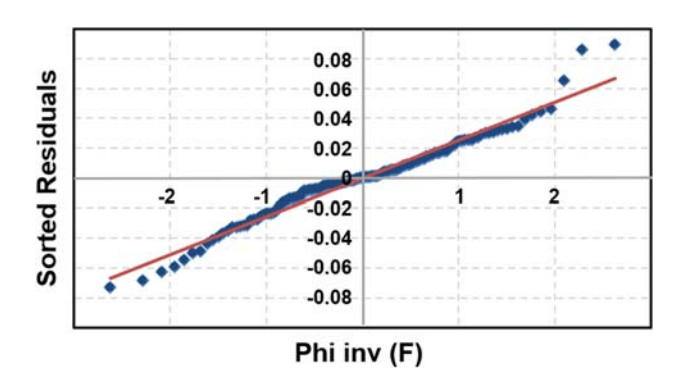


Fig. 15 Normal probability plot for model diagnosis

(i.e., the Hotelling T^2 statistics) is transformed to improve variance stabilization and reduce the heteroscedasticity as follows:

$$z = f(y) = \begin{cases} \frac{y^{\lambda} - 1}{\lambda}, & \lambda > 0\\ \log y, & \lambda = 0 \end{cases}$$
 (22)

The optimal value λ^* is selected to be -0.022 that provides the most parsimonious model with no unusual patterns in the residual plots. Based on the transformed data z, the resulted model is as follows:

$$Z = 11.802 - 68.77H - 0.0052P - 0.00698V + 208.82H*H + 0.000015P*P$$
(23)
+ 0.000002V*V

As shown in Table 1, the regression model yields the adjusted R-squared statistic of 94.76%, showing that the variations of process conditions are highly correlated with multifractal characteristics in the imaging profiles of AM builds. Note that H, P, V and H^2 , V^2 and P^2 have a p-value of zero. All the parameters are significant in the 95% confidence level. When we decrease the laser power, increase the scan velocity, and increase the hatch spacing from the nominal setting, Hotelling T^2 statistics will be increased. In other words, the heterogeneity of LPBF-AM images is increased, which indicates an increasing level of defects. As shown in Fig. 15, we use the normal probability plot for residual analysis and model diagnosis. The straight line shows that the residuals are approximately normal, which validates the regression model.

Journal of Manufacturing Science and Engineering

5 Conclusions

Advanced imaging technology is increasingly invested to increase information visibility and cope with system complexity in manufacturing processes. Massive image data provide rich information on the hidden dynamics of manufacturing processes and are conducive to improve the data-driven process monitoring and control. However, very little has been done to investigate the multifractal characteristics of image data for the purpose of process monitoring and quality control. This paper presents a joint multifractal and lacunarity analvsis to characterize and quantify image profiles from manufacturing processes (i.e., UPM and LPBF-AM). Experimental results show that the joint multifractal and lacunarity analysis not only effectively characterizes the surface finishes for quality control of UPM but also provides an effective predictive model to link process parameters with multifractal characteristics of in-process images acquired from the AM process. The proposed methodology has strong potentials to be applied for process monitoring and control of large amounts of image profiles in a variety of domains such as ultraprecision machining and additive manufacturing.

Acknowledgment

This work is supported in part by the NSF Center for e-Design (Lockheed Martin) at Penn State, and NSF (Grant Nos. CMMI-1617148 and CMMI-1719388). The author (H.Y.) also thanks Harold and Inge Marcus Career Professorship for additional financial support.

References

- Taniguchi, N., 1983, "Current Status in, and Future Trends of, Ultraprecision Machining and Ultrafine Materials Processing," CIRP Ann., 32(2), pp. 573–582.
- [2] Imani, F., Gaikwad, A., Montazeri, M., Rao, P., Yang, H., and Reutzel, E., 2018, "Process Mapping and In-Process Monitoring of Porosity in Laser Powder Bed Fusion Using Layerwise Optical Imaging," J. Manuf. Sci. Eng., 140(10), pp. 101009.
- [3] Lonardo, P., Lucca, D., and De Chiffre, L., 2002, "Emerging Trends in Surface Metrology," CIRP Ann., 51(2), pp. 701–723.
- [4] Kumara, S. R. T., and Bukkapatnam, S. T. S., 2007, "Characterization and Monitoring of Nonlinear Dynamics and Chaos in Manufacturing Enterprise Systems," Network Science, Nonlinear Science and Infrastructure Systems. International Series in Operations Research & Management, Vol. 102, T.L. Friesz, ed., Springer, Boston, MA, pp. 99–122.
- [5] Gültekin, M., Elsayed, E. A., English, J. R., and Hauksdóttir, A. S., 2002, "Monitoring Automatically Controlled Processes Using Statistical Control Charts," Int. J. Prod. Res., 40(10), pp. 2303–2320.
- [6] Singer, G., and Ben-Gal, I., 2007, "The Funnel Experiment: The Markov-Based SPC Approach," Qual. Reliab. Eng. Int., 23(8), pp. 899–913.
- [7] Imani, F., Gaikwad, A., Montazeri, M., Rao, P., Yang, H., and Reutzel, E., 2018, "Layerwise In-Process Quality Monitoring in Laser Powder Bed Fusion," ASME 2018 13th International Manufacturing Science and Engineering Conference, Volume 1: Additive Manufacturing; Bio and Sustainable Manufacturing, College Station, TX, June 18–22.
- [8] Yang, H., 2011, "Multiscale Recurrence Quantification Analysis of Spatial Cardiac Vectorcardiogram Signals," IEEE Trans. Biomed. Eng., 58(2), pp. 339–347.
- [9] Chen, Y., and Yang, H., 2016, "Numerical Simulation and Pattern Characterization of Nonlinear Spatiotemporal Dynamics on Fractal Surfaces for the Whole-Heart Modeling Applications," Eur. Phys. J. B, 89(181), pp. 1–16.
 [10] Ruschin-Rimini, N., Ben-Gal, I., and Maimon, O., 2013, "Fractal Geometry
- [10] Ruschin-Rimini, N., Ben-Gal, I., and Maimon, O., 2013, "Fractal Geometry Statistical Process Control for Non-Linear Pattern-Based Processes," IIE Trans., 45(4), pp. 355–373.
- [11] Mandelbrot, B. B., Passoja, D. E., and Paullay, A. J., 1984, "Fractal Character of Fracture Surfaces of Metals," Nature, 308(5961), pp. 721–722.
- 12] Yao, B., Imani, F., Sakpal, A. S., Reutzel, E. (Ted), and Yang, H., 2017, "Multifractal Analysis of Image Profiles for the Characterization and Detection of Defects in Additive Manufacturing," J. Manuf. Sci. Eng., 140(3), pp. 031014.
- [13] Davies, S., and Hall, P., 1999, "Fractal Analysis of Surface Roughness by Using Spatial Data," J. R. Stat. Soc. Ser. B, 61(1), pp. 3–37.
- [14] Jahn, R., and Truckenbrodt, H., 2004, "A Simple Fractal Analysis Method of the Surface Roughness," J. Mater. Process. Technol., 145(1), pp. 40–45.
- [15] Meisel, L. V., Johnson, M., and Cote, P. J., 1992, "Box-Counting Multifractal Analysis," Phys. Rev. A, 45(10), pp. 6989–6996.
- [16] Plotnick, R. E., Gardner, R. H., Hargrove, W. W., Prestegaard, K., and Perlmutter, M., 1996, "Lacunarity Analysis: A General Technique for the Analysis of Spatial Patterns," Phys. Rev. E, 53(5), pp. 5461–5468.
- [17] Allain, C., and Cloitre, M., 1991, "Characterizing the Lacunarity of Random and Deterministic Fractal Sets," Phys. Rev. A, 44(6), pp. 3552–3558.
- [18] Kan, C., and Yang, H., 2017, "Dynamic Network Monitoring and Control of in Situ Image Profiles from Ultraprecision Machining and Biomanufacturing Processes," Qual. Reliab. Eng. Int., 33(8), pp. 2003–2022.

APRIL 2019, Vol. 141 / 044501-7